PHYSICAL REVIEW MATERIALS **5**, 053401 (2021)

Precipitate growth kinetics under inhomogeneous concentration fields using a phase-field model

Y. Song ,[1,*] B. Radhakrishnan,[1,†] S. Gorti,[1] and R. Acharya[2]
[1]*Oak Ridge National Laboratory, 1 Bethel Valley Road, Oak Ridge, Tennessee 37830, USA*
[2]*Raytheon Technologies Research Center, 411 Silver Lane, MS 129-22, East Hartford, Connecticut 06118, USA*

(Received 17 December 2020; accepted 13 April 2021; published 17 May 2021)

We investigate precipitation dynamics in the presence of a local solute gradient using phase-field simulations. During the homogenization heat treatment of the solidified Inconel 718 alloy, high Nb concentration within the Laves phases or at the core of the secondary arms results in Nb diffusion into the γ matrix. The volume fraction and spatial distribution of precipitation during subsequent annealing can be controlled by tailoring the Nb concentration gradient in the matrix during homogenization. We use a surrogate Ni-Fe-Nb alloy for Inconel 718 to explore the growth dynamics of δ precipitates related to the local Nb concentration levels. The simulations indicate that in the presence of a Nb concentration gradient the growth rate of δ precipitates is higher than in a matrix of uniform average Nb concentration. The higher growth rate is a result of the higher local thermodynamic driving force at the interface between the solute-rich matrix and the δ interface. We propose a phenomenological model to describe the diffusion-controlled growth kinetics of the δ phase under a solute concentration gradient.

DOI: 10.1103/PhysRevMaterials.5.053401

I. INTRODUCTION

Additive manufacturing (AM) allows near-net fabrication of components with complex geometries using custom designs that are beyond the capabilities of conventional metal casting approaches [1,2]. AM is finding increasing application in many structural alloys, including nickel-base superalloys [3–7]. For nickel-base superalloys such as Inconel 718 (IN718), a postprocess heat treatment is applied to recover the target mechanical properties, which are improved by the precipitation of coherent phases such as γ'' [7–12].

In recent experimental studies [7,8], two steps of heat treatments are suggested for AM IN718. Solidified microstructures in IN718 contain undesirable Laves phases, which trap large quantities of Nb, which is required for the precipitation of the beneficial γ'' phase [4–8,13], and have detrimental effects on the mechanical properties [4,6,7]. Therefore homogenization to dissolve the Laves phase is an important first step in the postprocess annealing of AM IN718. When the dissolution of the Laves phase is complete, there are various levels of Nb concentration gradients in the matrix depending on the extent of homogenization [14]. During a subsequent aging treatment, the hardening phases precipitate within the γ matrix [7,8]. Precipitation in a concentration gradient is of interest because of the potential for creating gradient microstructures that are known to possess attractive mechanical properties compared to the homogeneous counterparts [15].

We use the phase-field (PF) method [16–18] to simulate the microstructure evolution during postprocess annealing in AM IN718. The PF method has emerged as a powerful technique to simulate microstructure evolution associated with solidification and solid-state phase transformations in multicomponent and multiphase alloys [16–24]. Solid-solid phase transformations are characterized by the presence of elastic strain fields associated with precipitate phases that show various levels of coherency with the matrix. The PF method is well suited to incorporate the effect of elastic strain fields, as well as the anisotropy in the matrix-precipitate interfacial energy, that influence the precipitate morphologies [22–27]. We perform simulations using the PF code MEUMAPPS (microstructural evolution using massively parallel phase-field simulations) that has been developed recently at the Oak Ridge National Laboratory (ORNL) [27] as a part of the Exascale Computing Program sponsored by the U.S. Department of Energy. We use this code to investigate the growth dynamics of precipitates in a surrogate Ni-Fe-Nb alloy for IN718.

This research presents important observations related to the precipitation kinetics under Nb gradients in IN718 using phase-field simulations, and the results indicate that the solute levels within the γ matrix are linked to the growth dynamics of the δ precipitates.

II. METHOD

In the MEUMAPPS-SS model, the total free energy $\mathcal{F}$ is described by the sum of the various components of the energy densities within a unit volume $\mathcal{V}$, i.e.,

$$\mathcal{F} = \int (f_b + f_{el} + f_{ch}) d\mathcal{V}. \tag{1}$$

The boundary energy f_b is the sum of the energy contributions at the diffuse inter-phase interface due to energy penalties caused by gradients in order parameters ϕ_v, corresponding to a δ variant v existing at the interface, and the boundary energies between phases [27]. With twelve variants of the δ phase [28],

---

[*] songy3@ornl.gov
[†] radhakrishnb@ornl.gov

the boundary energy is described as

$$f_b = \frac{1}{2}\sum_{v=1}^{12}[\nabla\phi_v]^T\kappa_v[\nabla\phi_v] + \sum_{v=1}^{12}\sum_{q>v}^{12}\omega_{vq}|\phi_v\,\phi_q| + \bar{\omega}\sum_{q=1}^{12}\phi_q\left(1-\sum_{v=1}^{12}\phi_v\right), \tag{2}$$

where κ_v is an anisotropic gradient coefficient of the δ variant, ω_{vq} is the height of an energy well that depends on the boundary width ($5\Delta x$), and $\bar{\omega}$ is the average height. The first term on the right-hand side of the above equation describes the gradient energy. The second and third terms are for the energies at the $\delta-\delta$ and the $\delta-\gamma$ boundaries, respectively. We use the interfacial energy $0.8\hat{x}+0.03\hat{y}+0.8\hat{z}$ [J μm^2/mol] for all variants to calculate the κ and ω terms following the method in Refs. [27,29].

For the elastic energy f_{el}, we use the Steinbach-Apel approach [22,24,27] that interpolates f_{el} as the sum of individual strain energies of phases through an interpolation function of the order parameter ϕ, which is given by

$$f_{el} = \sum_{v=1}^{12}h(\phi_v)f_{el}^{\delta,v} + \left[1-\sum_{v=1}^{12}h(\phi_v)\right]f_{el}^{\gamma}, \tag{3}$$

where $h(\phi)=\phi^3(6\phi^2-15\phi+10)$ is an interpolation function of the order parameter. The strain energy for a phase p is $f_{el}^p=\frac{1}{2}\epsilon_{ij}^{el,p}:C_{ijkl}^p:\epsilon_{kl}^{el,p}$, with the elastic strain $\epsilon_{ij}^{el}=\epsilon_{ij}^{\text{tot}}-\epsilon_{ij}^{*}$ calculated using the total strain $\epsilon_{ij}^{\text{tot}}$ and the transformation strain ϵ_{ij}^{*}. We used Khachaturyan's approach [25] that describes the total strain as the sum of the mean strain $\bar{\epsilon}_{ij}$ and the heterogeneous strain $\delta\epsilon_{ij}$, defined using the local displacement gradients, which is given by $\epsilon_{ij}^{\text{tot}}=\bar{\epsilon}_{ij}+\delta\epsilon_{ij}$. An iterative approach proposed by Hu and Chen [23,24] is used to compute the displacement field at every time step, which, in turn, is used to estimate the elastic energy field. Then the overall elastic strain between γ and δ is interpolated as $\epsilon_{ij}^{el}=\sum_v h(\phi_v)\epsilon_{ij}^{el,\delta,v}-[1-\sum_v h(\phi_v)]\epsilon_{ij}^{el,\gamma}$. The components of the elastic modulus tensor C are zero, except $(C_{11},C_{22},C_{44})=(203,150,135)$ for the γ matrix and $(C_{11},C_{12},C_{13},C_{33},C_{44},C_{66})=(260,96,97,280,109,143)$ for the δ variant in units of GPa.

The chemical energy f_{ch}^p of a phase p is described using quadratic functions of the element concentrations [26]. For the Ni-Fe-Nb system, the total chemical energy f_{ch} is interpolated using an expression similar to Eq. (3) [27], and the chemical energy of each phase p is given by

$$f_{ch}^p = A_1^p\left(X^{\text{Fe}}-A_4^p\right)^2 + A_2^p\left(X^{\text{Nb}}-A_5^p\right)^2 + A_3^p, \tag{4}$$

where X^{Fe} and X^{Nb} are the Fe and Nb concentrations in mole fractions, and A_i^p values are fitting parameters. The A_i^p parameters are obtained by fitting the Gibbs free energy from the THERMO-CALC software TCNI8 Ni-based superalloys [30]. For the δ precipitate growth, we consider the fixed temperature $T=850$°C. At this temperature we obtained the Gibbs free-energy data of the γ matrix with a resolution of 0.001 mole fraction within the ranges of $0.45\leqslant X^{\text{Fe}}\leqslant 0.75$ and $0.0\leqslant X^{\text{Nb}}\leqslant 0.15$ using THERMO-CALC. Similarly, we calculated energy values for the δ phase within $0.0\leqslant X^{\text{Fe}}\leqslant 0.2$ and $0.1\leqslant X^{\text{Nb}}\leqslant 0.3$. We used the same resolution of 0.001 for the free energy of the δ phase.

Then we fit the energy values as a function of X^{Fe} and X^{Nb} to Eq. (4) using PYTHON with the least-squares fitting method. The obtained A_i^p parameter sets are (A_1^p, A_2^p, A_3^p, A_4^p, A_5^p) = (21 654.6796, 188 869.6365,–67 323.8182, 0.19, 0.14) for the γ matrix and (86 533.8069, 365 879.3077,–77 299.9162, 0.09, 0.29) for the δ phase. The maximum errors of the fitting equations with respect to the THERMO-CALC data are 3.6% and 2.1% for the γ and δ phases, respectively, which show quantitative agreement with the energy data at $T=850\,^\circ$C. It is worth noting that because the Gibbs free energy is related to the temperature, the parameters should be estimated separately for different temperatures of interest. For example, the parameter set for γ becomes (28 300.9118, 185 748.1403,–86 558.1615, 0.3, 0.14) at $T=1100\,^\circ$C. The quadratic expression for the Gibbs free energy shown in Eq. (4) results in linear equations for the chemical potentials of Fe and Nb that make it convenient for the calculation of the interface concentrations required in the PF model using the Kim-Kim-Suzuki approach [20].

We solve the Ginzburg-Landau equation for the time evolution of the phase field of a variant ϕ_v [27],

$$\frac{\partial\phi_v(\rho,t)}{\partial t} = -L\left[\frac{1}{N}\sum_{v\neq q}\left(\frac{\delta\mathcal{F}}{\delta\phi_v(\rho,t)}-\frac{\delta\mathcal{F}}{\delta\phi_q(\rho,t)}\right)\right], \tag{5}$$

and the Cahn-Hilliard equation for the alloy components [27],

$$\frac{\partial X^c}{\partial t} = \vec{\nabla}\left(M^c\vec{\nabla}\frac{\partial f_{ch}}{\partial c}\right), \tag{6}$$

where L is the interface mobility, N is the number of phases coexisting at a position $\rho=(x,y,z)$, and M^c is the mobility of an element c. We use the Kim-Kim-Suzuki approach [20] to compute the solute concentrations at the various interphase interfaces based on the assumption of equal chemical potential of a solute within the phases at the interface. The governing equations are solved using a Fourier spectral method [31]. The P3DFFT library for the fast Fourier transform (FFT) was used to perform the calculations in a parallel computing environment [32]. We considered 12 variants of the δ phase that precipitate during heat treatments [7,8,14,26].

We used $\Delta x=1\times10^{-9}$ m (1 nm) for the grid spacing, $W=5\Delta x$ for the interface width, and $\Delta t=0.01$ s for the time step. In order to estimate the interface mobility L, we performed a separate simulation using δ precipitates growing under a higher $X^{\text{Nb}}=0.15$. The mobility is calculated using the procedure outlined in Ref. [33]. The mobility is sensitive to the mesh resolution. For the resolution of 1 nm used in this study, an average value computed using the above approach for different concentrations was $L=1.475\times10^{-10}$ m^3/J s, which we used in our simulations. In experimental measurements [26,34–36], the diffusion coefficient varies between $\sim10^{-16}$ and $\sim10^{-18}$. We used the smaller value of $D=10^{-18}$ m^2/s for both Fe and Nb elements.

Two simulation domains were considered: $N_x=N_y=N_z=210\Delta x$ for the large simulations involving multiple precipitates in Figs. 1 and 2, and $N_x=N_y=N_z=168\Delta x$ for simulations involving a single precipitate. Here N_x, N_y, and N_z are the number of grid points along the x, y, and z axes,

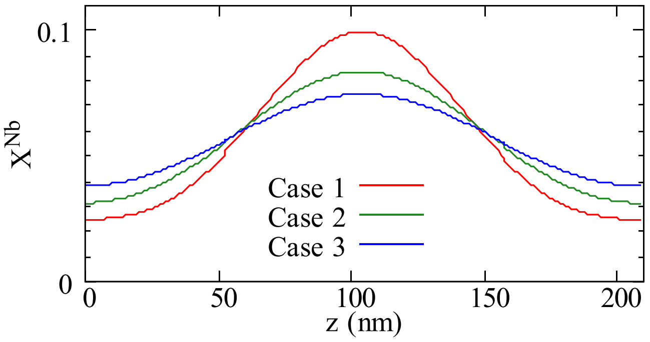

FIG. 1. Initial Nb profiles along the z axis. Three different profiles (red, green, and blue lines for cases 1, 2, and 3, respectively) are used as the initial conditions for PF simulations in Fig. 2. The simulation domain size along the z axis is 210 nm ($N_z = 210$ and $\Delta x = 1$ nm).

respectively. We used periodic boundary conditions along all the axes. Other material and elasticity parameters can be found elsewhere [26–29].

Our simulations were performed using 1764 IBM Power9 CPUs on Summit at Oak Ridge National Laboratory. The simulation with a large system size took about 3 h for 20 000 iterations. For a smaller system, it took about 4.5 h for 60 000 iterations. If a smaller Δx is used, it takes a longer time to perform a simulation relevant to our simulation size because it requires more grid points.

III. RESULTS AND DISCUSSION

A. Growth of multiple precipitates

During the homogenization heat treatment, segregated elements such as Nb slowly diffuse within the γ matrix. In addition, the dissolution of the Laves phase formed by the end of the solidification process leads to various levels of Nb [14]. Accordingly, if the homogenization step is not long enough, the segregated elements are not uniformly distributed within the matrix. The resulting nonuniform solute fields can affect the precipitate growth during the annealing step.

We use the THERMO-CALC software TCNI8 Ni-based superalloys [30] in conjunction with the PF method to model an inhomogeneous solute gradient within a secondary arm spacing. Based on the THERMO-CALC software, the ternary system of $X^{\mathrm{Fe}} = 0.483$ and $X^{\mathrm{Nb}} = 0.056$ shows reasonable agreement with both the solidification range and the volume fraction of the δ phase at $T = 850\,^{\circ}\mathrm{C}$ in IN718. We perform the Scheil solidification simulation of this system, and the result shows that the X^{Nb} (X^{Fe}) changes from 0.024 (0.523) to 0.123 (0.258) as the volume fraction of γ increases.

We use these values to estimate an inhomogeneous solute field for the initial solute profile. We assume that the high X^{Nb} is located at the center of the secondary arm spacing of 210 nm [37], and it linearly decreases along z according to $X^{\mathrm{Nb}}(x, y, z) = 0.123–0.001\,46|z - N_z/2|$ until $X^{\mathrm{Nb}} = 0.024$. We determine the slope to be $-0.001\,46$ to keep the average X^{Nb} as 0.056 within the simulation domain. In addition, X^{Fe} varies from 0.258 to 0.523 according to

$$X^{\mathrm{Fe}}(x, y, z) = 0.258 + 2.677(0.123 - X^{\mathrm{Nb}}), \qquad (7)$$

(a) Case 1

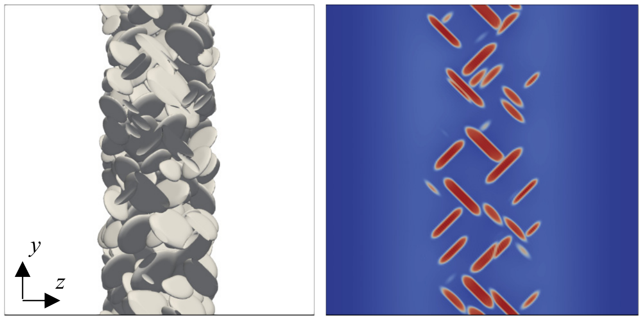

(b) Case 2

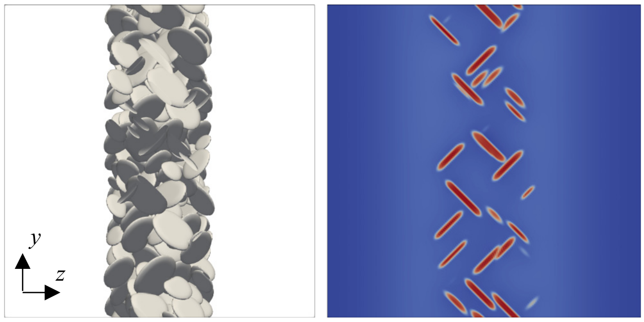

(c) Case 3

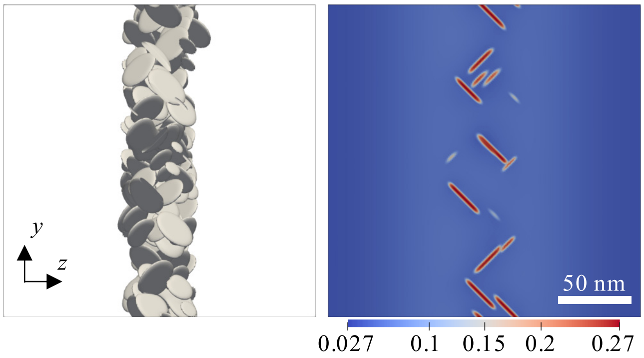

(d) δ fraction along the z axis

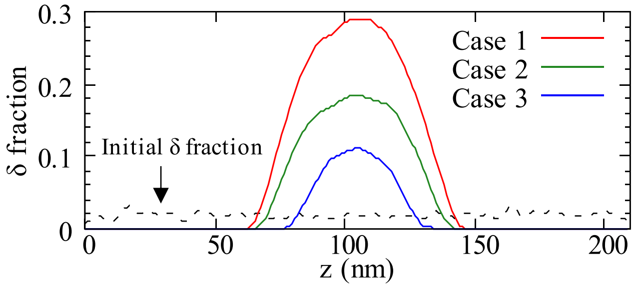

FIG. 2. Microstructures from phase-field simulations and concentration maps at a mid-2D section. Simulation results in (a), (b), and (c) used initial Nb profiles of cases 1, 2, and 3 in Fig. 1, respectively. Left microstructures show δ precipitates (silver) after 200 s at $T = 850\,^{\circ}\mathrm{C}$. Right color maps are the Nb fields at the midsection of the left microstructures. (d) δ fractions along the z axis for cases 1–3. In all simulations, δ seeds are distributed initially with fractions according to the black dashed line shown in (d).

which is linearly related to X^{Nb}. We let the solute fields evolve at $T = 1100\,^{\circ}\mathrm{C}$ within the γ matrix for 200 s, 600 s, and 1000 s, which correspond to the red, green, and blue lines in Fig. 1, respectively. These lines indicate the Nb profiles along the z axis. Then we use these solute profiles as the initial solute field and perform a simulation by randomly adding 1000 supercritical nuclei of the δ phase. We assigned nuclei to be one of the 12 δ variants chosen randomly and let them grow at $T = 850\,^{\circ}\mathrm{C}$.

When using a smaller radius of $1\Delta x$, most nuclei dissolved quickly even in the Nb-enriched central regions. We performed initial trials to determine the approximate nucleus size that would become critical for most of the central regions with Nb enrichment. A radius of $2\Delta x$ was found to be adequate based on these initial trials.

Figures 2(a)–2(c) show the δ phase precipitates (silver) within the γ matrix after 200 s, obtained using the three initial Nb profiles in Fig. 1. It can be seen from the microstructures shown on the left-hand side that the surviving δ precipitates are located near the central region. The δ nuclei located away from the center dissolve quickly because their growth is not energetically favorable due to an initially low Nb concentration.

The color maps on the right in Figs. 2(a)–2(c) show the Nb concentration fields at the midsection of the microstructures on the left. The higher Nb (red) regions indicate the δ precipitates. The δ precipitates for case 1 in Fig. 2(a) survive in greater numbers and grow to a larger size than those for the other cases in Figs. 2(b) and 2(c). In order to clarify the δ survival and growth due to different initial Nb profiles, we measure the δ fractions in Figs. 2(a)–2(c) along the z axis, namely,

$$\Phi(k) = \frac{\sum_{i=1}^{N_x}\sum_{j=1}^{N_y}\sum_{v=1}^{12}\phi_v(i,j,k)}{N_x \times N_y}, \tag{8}$$

where i, j, and k are the coordinates of a grid point along the x, y, and z axes, respectively. In all three cases, the initial δ fraction is the same as the black dashed line in Fig. 2(d). Due to the initial Nb distribution, the fraction $\Phi(k)$ decreases from case 1 (red solid line) to case 2 (green solid line) and case 3 (blue solid line) in Fig. 2(d).

The greater fraction of surviving precipitates in case 1 is linked to the initially higher Nb concentration near the midsection. The higher Nb concentration leads to higher nucleation density because of the reduced activation energy [38]. In addition, the higher Nb concentration leads to a greater driving force for precipitate growth.

It is worth noting that the survival of the δ is related to the critical nucleus size for a given Nb concentration. The width of the δ precipitation region in the center will depend on the size of the nucleus used in simulations. If we had introduced nuclei of a larger size, the δ precipitation zone would have been wider because more nuclei would have survived at lower Nb concentrations. While we introduced nuclei with a fixed size in our simulations, nucleation could also be modeled through random perturbation of the order parameters of different variants using a Langevin noise. The width of the δ precipitation region in this case would be influenced by the choice of the parameters used in the Langevin noise model. This will be investigated further in future studies.

These results suggest that the δ precipitate growth is related to the local Nb concentration. In addition, a local solute gradient could also influence the growth kinetics of a precipitate. In order to quantify the effect of the local solute level on the precipitation kinetics, we perform simulations using a single precipitate that grows under different solute gradients.

B. Growth of a single precipitate

For the simulation of a single δ precipitate growth, one supercritical seed with a radius of $2\Delta x$ is initially located at the center of the simulation domain. We first consider a uniform distribution of $X^{\mathrm{Nb}} = 0.1$ within the matrix. Based on Eq. (7), $X^{\mathrm{Fe}} = 0.32$ is imposed. In order to minimize the incubation time associated with nucleation, we use a high $X^{\mathrm{Nb}} = 0.24$ and a low $X^{\mathrm{Fe}} = 0.047$ within the δ seed, based on the known levels of Nb and Fe inside the δ phase from the TCNI8 database [30].

The δ precipitate exhibits a platelike morphology, and hence we can describe its morphology based on its radius r within the (111) plane and thickness h orthogonal to the plane. Under steady-state conditions, the interfaces normal to r and h should satisfy diffusion-controlled growth dynamics based on the power law $g_0 t^{1/2}$ [39], where g_0 is the growth constant. Including the elastic strain affects only the growth constant, and the power-law exponent remains 1/2 [40,41].

Figure 3(a) shows the δ (silver) at $t = 300$ s. In (a), the δ shape as shown along the blue (111) plane is not a perfect ellipse, because the shape is influenced by elastic energy and anisotropy in the interfacial energy. We interpolate interface positions ($\phi = 0.5$) on the plane using the PARAVIEW program [42]. At $t = 0$ s, the program interpolated 21 positions. As the δ grows, it calculates more interface positions. For example, we obtained 907 positions for the δ in Fig. 3(a). We averaged the positions to compute the radius values for Fig. 3(b).

In Fig. 3(b) we plot $r^2 - r_0(t_0)^2$ as a function of time $t - t_0$ with a reference time t_0. We averaged the interface positions measured in the (111) habit plane to calculate the radius $r = r(t)$ at a time t. From the time when it reaches the steady state, the precipitate growth would show the power-law growth and thus $r^2 - r_0(t_0)^2 \sim t - t_0$ [40,41]. It is difficult to predict when the precipitate reaches the steady state, and hence we use three reference times, $t_0 = 0$ s, 150 s, and 300 s, and, at those times, the radii are $r_0(t_0) = 1.7$, 29.2, and 52.4 nm, respectively. In the plot, solid lines are for simulation results and dashed lines are the fitted linear guide lines. The insert in (c) is a log-log plot showing a linear fit.

The initial evolution of the δ phase occurs under the artificial nucleation conditions, and it takes some time for the conditions to reach a thermodynamically consistent state of growth. During this stage, the δ growth rate (black line) is faster than the linear slope expected from a purely diffusion-controlled growth. As time proceeds (blue and red lines), it approaches the diffusion-controlled growth limit. While we measure the radius only up to ~500 s, since the δ grows out of the simulation box at longer simulation times, we expect the power-law exponent to be satisfied ($p = 1$) under such conditions.

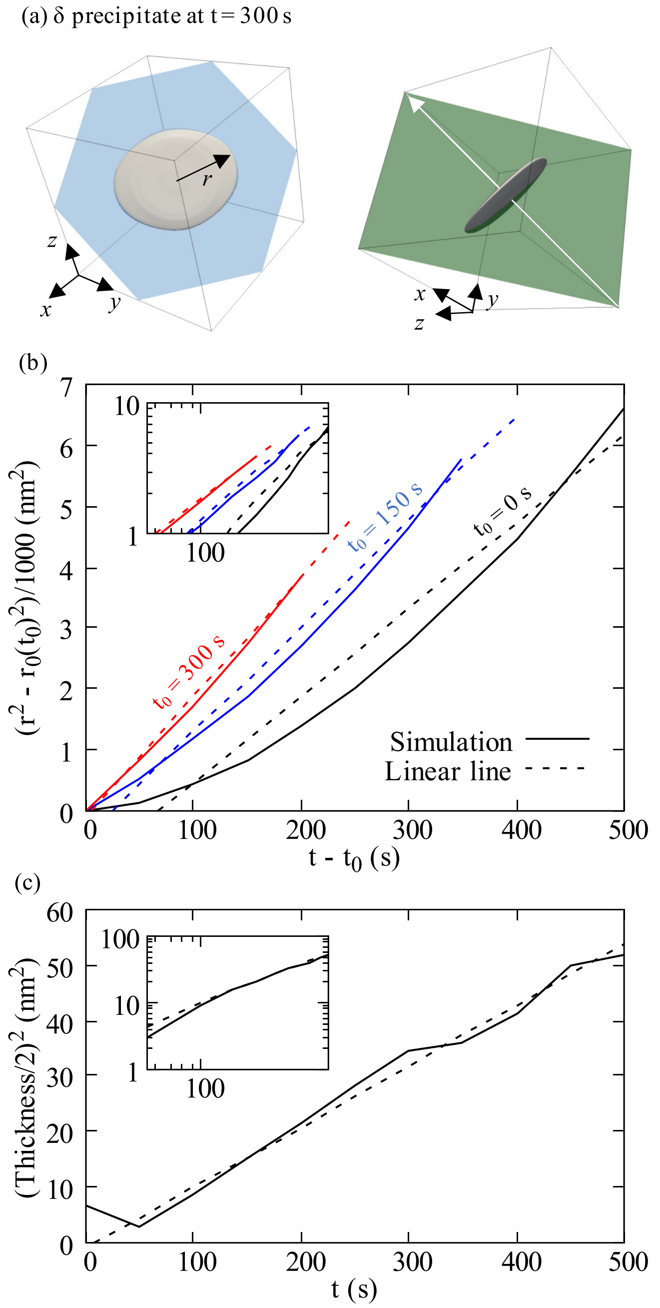

FIG. 3. Radius and thickness of a δ precipitate as a function of time under initially uniform solute fields. The left image in (a) shows a radius r of the δ (silver) within the blue (111) plane. On the right, the ϕ profile along the white arrow across the center of the δ on the green $(10\bar{1})$ plane is used to measure the thickness. (b) Shows $r^2 - r_0(t_0)^2$ of a δ precipitate, where r is the average radius and r_0 is the radius at a reference time t_0. We use three different $r_0(t_0)$ [nm] = 1.7 for $t_0 = 0$ s (black line), 29.2 for $t_0 = 150$ s (blue line), and 52.4 for $t_0 = 300$ s (red line). (c) The square of the half thickness as a function of time. In both plots, solid and dashed lines are for the simulation results and linear fits, respectively. The insets show the log-log plots.

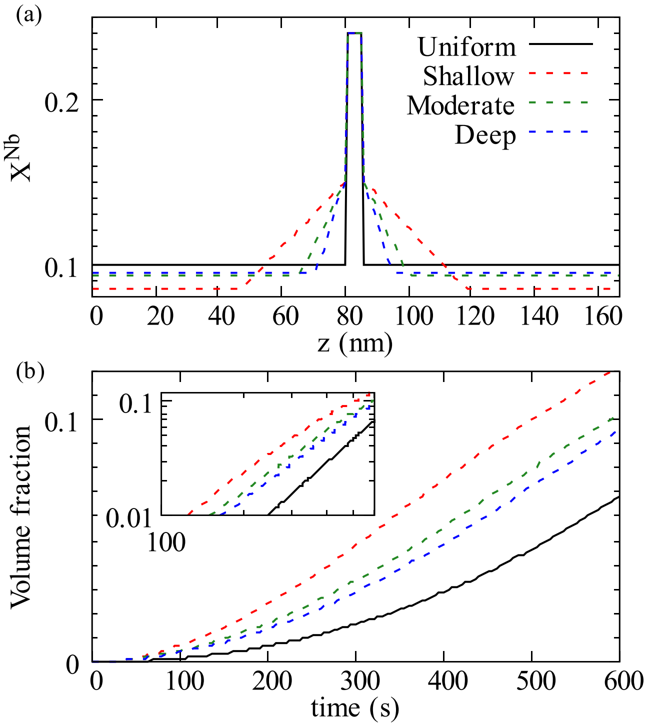

FIG. 4. Growth of a δ precipitate under different Nb gradients. (a) Initial Nb profiles along the z axis at the center using different gradient slopes. The δ nucleus is located at the center with a high $X^{\mathrm{Nb}} = 0.24$. Black solid line is for the uniform $X^{\mathrm{Nb}} = 0.1$ field within the matrix. Red, green, and blue dashed lines are for the gradients of ±0.002, ±0.004, and ±0.006, respectively. (b) The volume fractions at different times. The inset is for the log-log plot.

We used PARAVIEW to estimate the thickness of the δ. We obtained the ϕ profile along the white arrow on the $(10\bar{1})$ plane, which is the green plane in the right image of Fig. 3(a). This arrow passes through the center of the δ. We measured two interface positions from the profile, and the distance between them was the thickness. Similarly, we obtained additional ϕ profiles along four other lines that are orthogonal to the (111) plane. Those lines are $\pm 10\Delta x$ apart from the white arrow along the x and y axes.

We averaged the measured thickness values of the δ in Fig. 3(c). The dashed line is the linear fit using the simulation data (black solid line) from $t = 50$ s. The thickness h in the simulation shows steady-state growth according to $(0.5h)^2 \sim t$ (dashed line) from the beginning. We assume that due to the slow thickness growth, the solute profiles quickly approach the steady state. Accordingly, we expect the diffusion-controlled growth to be reached fairly early in the process.

We consider the precipitate growth under three different initial Nb gradients as shown in Fig. 4(a). We also introduce a high $X^{\mathrm{Nb}} = 0.24$ and a low $X^{\mathrm{Fe}} = 0.047$ within the δ to minimize the influence of the nucleation kinetics. Inside the matrix, $X^{\mathrm{Nb}} = 0.15$ at the center region where a precipitate is located. Otherwise, as illustrated in Fig. 4(a), X^{Nb} decreases away from the interface along the z axis with shallow (red dashed line), moderate (green dashed line), and deep (blue dashed line) gradients until X^{Nb} reaches the minimum value. The minimum X^{Nb} is estimated by using the bilinear interpolation to keep the average $X^{\mathrm{Nb}} = 0.1$. X^{Fe} is determined using Eq. (7), and its average value remains $X^{\mathrm{Fe}} = 0.32$. The gradient profiles represent solidification microstructures with microsegregation of Nb corresponding to different cooling

(a) Uniform (b) Shallow gradient

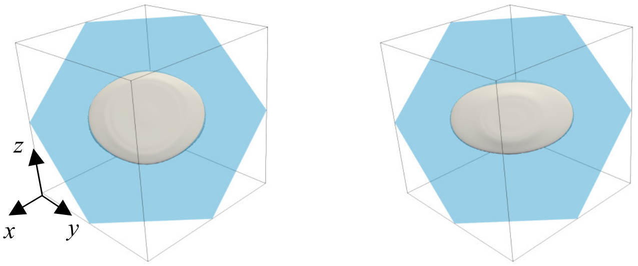

(c) Moderate gradient (d) Deep gradient

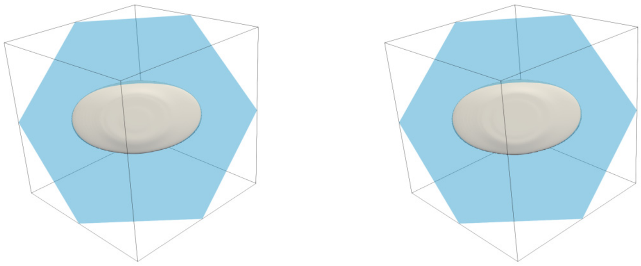

FIG. 5. δ precipitates for the volume fraction of $V_f = 0.015$. The volume fraction is reached around $t = 295.21$ s for the uniform (a), 154.02 s for the shallow (b), 190.97 s for the moderate (c), and 209.51 s for the deep gradient cases (d). Blue plane indicates the (111) plane.

rates of IN718 that lead to different Nb gradients in the matrix coexisting with the Laves phase.

Figure 4(b) exhibits the volume fractions (V_f) as a function of time. Simulation results show that the δ phase under a Nb gradient (dashed lines) grows faster than under the uniform $X^{\mathrm{Nb}} = 0.1$ (solid line).

We have examined the δ morphologies due to the different solute gradients, as shown in Fig. 5 when the volume fraction of the δ phase is $V_f = 0.015$. The black box indicates the simulation domain, and the gray shapes are the δ. Under the initially uniform condition, the δ precipitate attains the volume fraction $V_f = 0.015$ at $t = 295.21$ s (a). The precipitate can reach the same volume fraction earlier when a gradient is imposed, i.e., $t = 154.02$ s for the shallow (b), 190.97 s for the moderate (c), and 209.51 s for the deep gradients (d).

Due to anisotropy in the interfacial and the elastic energies, the δ precipitate has a noncircular shape along the (111) plane (blue plane) under the uniform condition as shown in Fig. 4(a). However, we observe that the shape of the δ plates is different in the presence of gradients in the Nb concentration. We measure the angle of the maximum radius of the δ plate with respect to the z axis, and it is 85.6° for the uniform case. The angle is slightly increased to 89.2° when the gradient has been imposed, as shown in Figs. 4(b)–4(d). For all cases where a Nb gradient is initially imposed in the z direction, the Nb-enriched region is located at the center of the domain, which is asymmetric with respect to the (111) plane. Hence the δ becomes elongated along the Nb-enriched region due to the higher thermodynamic driving force. Accordingly, the ratios between the maximum and minimum radii of the δ plates for the gradient cases in Figs. 5(b)–5(d) are 1.76, 1.90, and 1.84, respectively. These values are considerably higher than the corresponding ratio of 1.26 for the uniform condition case in Fig. 5(a).

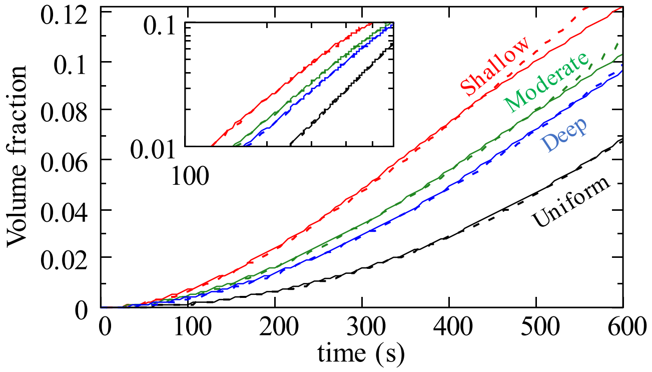

FIG. 6. Volume fraction as a function of time from the simulations (solid lines) and prediction (dashed lines). Dashed lines are the predicted growth rates using Eq. (10). For the uniform case, the equation becomes Eq. (9) due to $F_R(t) = 1$. The inset is for the log-log scale.

Since the interface of the precipitate follows a parabolic growth of $t^{1/2}$ at steady state [38,40,41], the volume of the precipitate should increase based on the power-law growth exponent of 3/2 [39,43]. In our simulations, the δ precipitate grows as a noncircular plate. The volume during growth is mainly related to the mean radius of the plate and its thickness. We have shown earlier that the thickness follows a diffusion-controlled growth with a growth exponent of roughly 0.5, while the growth exponent of the radius is higher at the initial transient stage during which thermodynamic consistency is being approached [Fig. 3(a)]. Hence, the power-law exponent s_g for the volume fraction given by

$$V_f = V_0 t^{s_g} \tag{9}$$

is not 1.5 when evaluated from $t = 0$. When we fit the simulation results for the uniform condition (black solid line in Fig. 6) to Eq. (9), the power-law exponent becomes $s_g = 2.15$ with $V_0 = 7.24 \times 10^{-8}$ (black dashed line).

The higher growth rate in the presence of a Nb gradient, with a higher Nb at the precipitate-matrix interface shown in Fig. 4(a), is probably due to the higher thermodynamic driving force associated with the higher Nb concentration. Accordingly, we can modify Eq. (9) by introducing an additional contribution of $F_R(t)$ as

$$V_f = F_R(t)\, V_0\, t^{s_g} \tag{10}$$

to incorporate the effect of local solute concentration and the associated thermodynamic driving force on the volume fraction.

The term $F_R(t)$ would be related to the free energy and the diffusion dynamics. The chemical free energy is much higher than the elastic strain energy and thus provides the main contribution to the modification. The effect of Nb concentration on the driving force for growth is obtained through Eq. (4). In addition, the precipitate growth would approach the growth kinetics under a uniform field as the solute field homogenizes. Therefore the value approaches $F_R(t) \rightarrow 1$ after a long time. Based on our simulation results, we suggest an expression for $F_R(t)$ to describe the δ growth under a solute gradient, which is

$$F_R(t) = (X_r^2 - b_0[1 - \exp(-t/\tau)])^{s_f}, \tag{11}$$

where the ratio $X_r = X_{\max}^{\mathrm{Nb}}/\bar{X}^{\mathrm{Nb}}$ is between the effective maximum and the average Nb concentrations, which are related to the free-energy contribution. For the simulation with the shallow gradient, those are $X_{\max}^{\mathrm{Nb}} = 0.15$ and $\bar{X}^{\mathrm{Nb}} = 0.1$. The constant b_0 is determined by $b_0 = X_r^2 - 1$, and hence the function $F_R(t)$ approaches towards 1 as time elapses. For the uniform case, the constants in the above equation become $X_r = 1$ and $b_0 = 0$, which leads to $F_R(t) = 1$. Then Eq. (10) is the same as the power-law growth in Eq. (9). We assume that the precipitate growth follows the same power law of $s_f = s_g = 2.15$ for the uniform case. The characteristic time τ is linked to the diffusion dynamics. We use the best-fit approximation to obtain τ within the simulation results before 400 s for the shallow gradient simulation (red solid line in Fig. 6). The modified V_f in Eq. (10) with the fitted $\tau = 501$ s (red dashed line) agrees well with the simulation result.

For the predictions of the moderate (green dashed line) and deep (blue dashed line) gradients, we use $X_r = 1.34$ and 1.28, respectively. The concentration at the interface changes quickly with a high gradient, so the effective maximum Nb concentration needs to be lower than that for the shallow gradient, which leads to a smaller X_r ratio. The other parameters s_f and τ are related to the diffusion, and they are consistent in our system. As shown in Fig. 6, the predictions for the other gradients also show quantitative agreement with the simulation results.

At a longer time, the δ growth slows down in the simulation. This is because, as the precipitate grows outside the simulation domain, one side of the δ approaches the other side due to the periodic boundary. We expect that the simulation result would follow the predicted dashed line better if the simulation domain size were larger. It is worth noting that the power-law exponents s_g and s_f would be 1.5 under steady-state conditions because diffusion controls the interface growth.

IV. CONCLUSIONS

We performed PF simulations of solid-state phase transformations to investigate precipitate growth kinetics within the γ matrix using a surrogate Ni-Fe-Nb alloy for IN718. Our simulations indicate that both the nucleation and growth rates of the δ phase are accelerated due to the solute enrichment associated with interdendritic segregation of Nb in a Ni-Fe-Nb alloy used as a surrogate for IN718. We additionally investigated the growth dynamics of a single precipitate under various solute gradients indicative of different cooling conditions characteristic of those expected under AM conditions. Within initially uniform solute fields, the interface growth of a precipitate shows the power-law growth exponent close to $1/2$ at steady state, as predicted for diffusion-controlled growth [40,41]. Due to the slow growth of the thickness of the δ phase, it reaches the exponent of $1/2$ quickly. On the other hand, it takes a longer time for the δ radius to approach the steady-state growth rate. At an intermediate state before reaching the steady state, the δ radius grows faster for nonstabilized elastic and solute fields. Accordingly, the volume fraction shows a different growth exponent of $s_g = 2.15$ in Eq. (9), instead of the predicted value of 3/2 [39,43]. With $\bar{X}^{\mathrm{Nb}} = 0.15$ for the initial δ-matrix interface Nb concentration, a shallow gradient results in the precipitate interface facing a higher Nb for a longer time, which results in a faster interface growth due to the higher thermodynamic driving force. In addition, the asymmetric interface growth linked to the local Nb level leads to a precipitate morphology different from that under the homogenized concentration field. In order to describe the volume fraction of a precipitate under a solute gradient, we introduce a phenomenological function that is linked to the free energy and the diffusion dynamics. The modified prediction including the phenomenological approach agrees well with the simulation result (Fig. 6).

Advanced manufacturing processes such as additive manufacturing are currently being used to manufacture structural components. The solidification microstructure under such processing conditions is characterized by solute enrichment, such as Nb enrichment in the Ni-base superalloy 718. Nb enrichment plays a critical role in the type, morphology, and spatial distribution of precipitates that form during postprocess heat treatment of these components [5,14,44,45]. The simulations presented here highlight the relationship between precipitate growth kinetics and the local solute conditions characteristic of those expected under AM solidification conditions. The results are relevant to the design of customized heat treatment for AM components in alloy 718, especially the development of gradient microstructures that show considerable improvement in the mechanical properties compared to materials with uniform microstructures.

ACKNOWLEDGMENTS

This research was supported by the High-Performance Computing for Manufacturing (HPC4Mfg) program sponsored by the Advanced Manufacturing Office of the U.S. Department of Energy (DOE), and by the Exascale Computing Project (17-SC-20-SC), a collaborative effort of the U.S. DOE Office of Science and the National Nuclear Security Administration. This research used resources of the Oak Ridge Leadership Computing Facility, which is a DOE Office of Science User Facility supported under contract DE-AC05-00OR22725. This work has been partially supported by U.S. DOE. ORNL is managed by UT-Battelle, LLC, under Contract No. DE-AC05-00OR22725 for the U.S. DOE. The U.S. government retains and the publisher, by accepting the article for publication, acknowledges that the U.S. government retains a nonexclusive, paid-up, irrevocable, worldwide license to publish or reproduce the published form of this manuscript, or allow others to do so, for U.S. government purposes. DOE will provide public access to these results of federally sponsored research in accordance with the DOE Public Access Plan [46].

[1] W. E. Frazier, J. Mater. Eng. Perform. **23**, 1917 (2014).

[2] W. J. Sames, F. A. List, S. Pannala, R. R. Dehoff, and S. S. Babu, Int. Mater. Rev. **61**, 315 (2016).

[3] Z. Wang, K. Guan, M. Gao, X. Li, X. Chen, and X. Zeng, J. Alloys Compd. **513**, 518 (2012).

[4] A. T. Polonsky, M. P. Echlin, W. C. Lenthe, R. R. Dehoff, M. M. Kirka, and T. M. Pollock, Mater. Charact. **143**, 171 (2018).

[5] H. Song, T. McGaughy, A. Sadek, and W. Zhang, Additive Manufacturing **26**, 30 (2019).

[6] Y. Chen, Y. Guo, M. Xu, C. Ma, Q. Zhang, L. Wang, J. Yao, and Z. Li, Mater. Sci. Eng. A **754**, 339 (2019).

[7] T.G. Gallmeyer, S. Moorthy, B. B. Kappes, M. J. Mills, B. Amin-Ahmadi, and A.P. Stebner, Additive Manufacturing **31**, 100977 (2020).

[8] H. Song, Ph.D. thesis, The Ohio State University, 2016.

[9] J. M. Oblak, D. F. Paulonis, and D. S. Duvall, Metall. Trans. **5**, 143 (1974).

[10] M. C. Chaturvedi and Y.-f. Han, Metal Science **17**, 145 (1983).

[11] M. Sundararaman, J. B. Singh, and P. Mukhopadhyay, Scr. Metall. Mater. **29**, 557 (1993).

[12] C. Slama and M. Abdellaouib, J. Alloys Compd. **306**, 277 (2000).

[13] G. A. Knorovsky, M. J. Cieslak, T. J. Headley, A. D. Romig, Jr., and W. F. Hammetter, Metall. Trans. A **20**, 2149 (1989).

[14] D. Deng, R. L. Peng, H. Söderberg, and J. Moverare, Mater. Design **160**, 251 (2018).

[15] Y. Wang, G. Yang, W. Wang, X. Wang, Q. Li, and Y. Wei, Sci. Rep. **7**, 10954 (2017).

[16] L. Q. Chen, Annu. Rev. Mater. Res. **32**, 113 (2002).

[17] W. J. Boettinger, J. A. Warren, C. Beckermann, and A. Karma, Annu. Rev. Mater. Res. **32**, 163 (2002).

[18] N. Moelans, B. Blanpain, and P. Wollants, Calphad **32**, 268 (2008).

[19] I. Steinbach, Annu. Rev. Mater. Res. **43**, 89 (2013).

[20] S. G. Kim, W. T. Kim, and T. Suzuki, Phys. Rev. E **60**, 7186 (1999).

[21] I. Steinbach, F. Pezzolla, B. Nestler, M. Seeßelberg, R. Prieler, G. J. Schmitz, and J. L. L. Rezende, Physica D **94**, 135 (1996).

[22] I. Steinbach and M. Apel, Physica D **217**, 153 (2006).

[23] S. Y. Hu and L. Q. Chen, Acta Mater. **49**, 1879 (2001).

[24] A. Durga, P. Wollants, and N. Moelans, Modelling Simul. Mater. Sci. Eng. **21**, 055018 (2013).

[25] A. G. Khachaturyan, *Theory of Structural Transformations in Solids* (Wiley, New York, 1983).

[26] N. Zhou, D. C. Lv, H. L. Zhang, D. McAllister, F. Zhang, M. J. Mills, and Y. Wang, Acta Mater. **65**, 270 (2014).

[27] B. Radhakrishnan, S. Gorti, and S. S. Babu, Metall. Mater. Trans. A **47**, 6577 (2016).

[28] S. Mahadevan, S. Nalawade, J. B. Singh, A. Verma, B. Paul, and K. Ramaswamy, in *7th International Symposium Superalloy 718 and Derivatives, 2010*, edited by E. A. Ott *et al.* (TMS, 2010), p. 737.

[29] R. Shi and Y. Wang, Acta Mater. **61**, 6006 (2013).

[30] J. O. Andersson, T. Helander, L. Höglund, P. F. Shi, and B. Sundman, Calphad **26**, 273 (2002).

[31] L. Q. Chen and J. Shen, Comput. Phys. Commun. **108**, 147 (1998).

[32] D. Pekurovsky, SIAM J. Sci. Comput. **34**, C192 (2012).

[33] S. G. Kim, Acta Mater. **55**, 4391 (2003).

[34] A. Devaux, L. Nazé, R. Molins, A. Pineau, A. Organista, J. Y. Guédou, J. F. Uginet, and P. Héritiere, Mater. Sci. Eng. A **486**, 117 (2008).

[35] R. V. Patil and G. B. Kale, J. Nucl. Mater. **230**, 57 (1996).

[36] M. S. A. Karunaratne and R. C. Reed, Defect and Diffusion Forum **237-240**, 420 (2005).

[37] B. Radhakrishnan, S. B. Gorti, J. A. Turner, R. Acharya, J. A. Sharon, A. Staroselsky, and T. El-Wardany, Metals **9**, 14 (2019).

[38] F. Liu, F. Sommer, C. Bos, and E. J. Mittemeijer, Intern. Mater. Rev. **52**, 193 (2007).

[39] C. Zener, J. Appl. Phys. **20**, 950 (1949).

[40] V. J. Laraia, W. C. Johnson, and P. W. Voorhees, J. Mater. Res. **3**, 257 (1988).

[41] R. Sankaran and C. Laird, Acta Metall. **22**, 957 (1974).

[42] J. Ahrens, B. Geveci, C. Law, *ParaView: An End-User Tool for Large Data Visualization* (Visualization Handbook, Elsevier, 2005).

[43] G. P. Krielaart, J. Sietsma, and S. van der Zwaag, Mater. Sci. Eng. A **237**, 223 (1997).

[44] E. A. Lass, M. R. Stoudt, M. E. Williams, M. B. Katz, L. E. Levine, T. Q. Phan, T. H. Gnaeupel-Herold, and D. S. NG, Metall. Mater. Trans. A **48**, 5547 (2017).

[45] E. A. Lass, M. R. Stoudt, M. B. Katz, and M. E. Williams, Scripta Mater. **154**, 83 (2018).

[46] http://energy.gov/downloads/doe-public-access-plan.